Microstructure and mechanical properties of an oxide-dispersed ultrafine-grained maraging steel

Shi, Bowen; Zeng, Tianyi; Tao, Nairong; Shi, Xianbo; Zhang, Jiarong; Wang, Wei; der Zwaag, Sybrand van; Shan, Yiyin; Yan, Wei

DOI
10.1016/j.jmrt.2025.06.216

Publication date
2025

Document Version
Final published version

Published in
Journal of Materials Research and Technology

Journal of Materials Research and Technology 37 (2025) 3075–3088

Contents lists available at ScienceDirect

Journal of Materials Research and Technology

journal homepage: www.elsevier.com/locate/jmrt

Microstructure and mechanical properties of an oxide-dispersed ultrafine-grained maraging steel

Bowen Shi [a,b], Tianyi Zeng [c], Nairong Tao [d], Xianbo Shi [b], Jiarong Zhang [b], Wei Wang [b], Sybrand van der Zwaag [e], Yiyin Shan [b], Wei Yan [b,*]

[a] School of Materials Science and Engineering, Northeastern University, Shenyang, 110819, China
[b] Shi-changxu Innovation Center for Advanced Materials, Institute of Metal Research, Chinese Academy of Sciences, Shenyang, 110016, China
[c] School of Packaging and Materials Engineering, Hunan University of Technology, Zhuzhou, 412007, China
[d] Shenyang National Laboratory of Materials Science, Institute of Metal Research, Chinese Academy of Sciences, Shenyang, 110016, China
[e] Faculty of Aerospace Engineering, Delft University of Technology, Delft, Netherlands

ARTICLE INFO

Handling Editor: P Rios

Keywords:
Maraging steel
Ultrafine grains
Nano-oxides
Variant selection
Martensitic transformation

ABSTRACT

A novel oxide-dispersed strengthened T250 maraging steel (ODS-T250 steel) was prepared by mechanical ball milling followed by hot isostatic pressing. Martensitic transformation behavior, ultrafine-grained martensite microstructure and tensile properties of the ODS-T250 steel were compared to its oxide-free counterpart (T250 steel). The results indicated that ODS-T250 steel exhibited excellent microstructural thermal stability, maintaining an effective grain size of 0.348 μm even after quenching from 1200 °C, whereas T250 steel exhibited a much larger grain size of 5.473 μm. After quenching, the ODS-T250 steel showed significantly distinct variant selectivity, and its martensite morphology was unprecedented equiaxed structure rather than typical lath-type. Statistical analysis revealed that there was only a single variant formed when the prior austenite grain size (PAGS) was below 0.43 μm. Moreover, the martensite start (Ms) temperature of ODS-T250 steel was lower than the T250 steel due to its ultrafine PAGS and the dispersed oxide particles. The refinement of PAGS and the presence of oxide particles led to a simultaneous improvement in both strength and ductility of ODS-T250 steel.

1. Introduction

Maraging steels are a family of ultra-high strength steels characterized by an extremely low carbon content and significant age-hardening in of their Fe–Ni lath martensitic structure [1]. Generally, lath martensite prevails in maraging steels after quenching from the solid solution temperature. Only a small fraction of retained austenite present in the form of films between martensite laths after the post-quenching deep cryogenic treatment. Subsequently, aging treatment is leads to the formation of nano-sized η-Ni_3(Ti, Mo), B2–Ni(Fe, Ti), and Laves-$(Fe, Cr)_2Mo$ phases in the martensite matrix [2–4]. These precipitates enable maraging steels to achieve ultra-high strengths, rendering them suitable for applications such as automotive components, aircraft landing gears, cryogenic tanks and so on. However, the pursuit of ultra-high strength often negatively affects ductility [5]. For maraging steels, overcoming the trade-off between strength and ductility remains a significant challenge once the yield strength exceeds 2000 MPa [3,6,7].Grain refinement is an effective strategy to enhance both strength and ductility in maraging steels [8]. However, conventional methods struggle to produce ultrafine-grained maraging steels [9]. Dynamic recrystallization during hot-working has been widely reported to refine grain size in steels [10], but this route can only produce grains of only tens of microns in maraging steels due to the relatively prolonged homogenizing annealing time and limited deformation resulting from their poor hot workability. Recent studies have attempted to use cyclic quenching treatments to refine prior austenite grains in steel. For example, Zhou et al. [11] performed the cyclic quenching treatment on a 2.3 GPa maraging steel, doubling the Charpy V-notch impact energy despite no significant refinement of prior austenite grains. Moreover, Wang et al. [12] obtained an excellent strength-ductility balance in 18CrNiMo7-6 steel through the cyclic quenching treatment, even though the prior austenite grain size (PAGS) was refined from an initial 14 μm to approximately 3 μm, highlighting the inherent limitations of this approach. Severe plastic deformation (SPD) techniques, such as high-pressure torsion (HPT) [13], equal channel angular pressing (ECAP) [14], and accumulative roll pressing (ARB) [15], are also very

* Corresponding author. Institute of Metal Research, Chinese Academy of Sciences, Shenyang, 110016, China.
E-mail address: weiyan@imr.ac.cn (W. Yan).

https://doi.org/10.1016/j.jmrt.2025.06.216
Received 13 May 2025; Received in revised form 23 June 2025; Accepted 28 June 2025
Available online 30 June 2025

effective means for achieving ultrafine grains. During SPD, high shear stress is applied to the material, leading to a proliferation of dislocation formation and a continuous increase in dislocation density. These dislocations entangle to form numerous small dislocation cells, which, under continued deformation, evolve into sub-grains with independent slip systems. Further application of stress transforms these sub-grains into new grains, characterized by either high or low angle grain boundaries [16,17]. This process promotes the fragmentation and refinement of the original grains, ultimately resulting in ultrafine grains with nanometer or submicron scale dimensions. Although ultrafine grains can be prepared by SPD method, the ultrafine grains rapidly coarsen during the solid solution treatment, making it difficult to maintain the stability of the prior austenite grains [18].

Currently, oxides dispersion strengthened (ODS) steel has become the leading candidate of structural material for future nuclear reactors, due to the presence of nano-sized oxide particles well dispersed within the matrix. It can restrain the dislocations movement and act as sinks for irradiation-induced defects [19]. Thanks to these small oxide particles, an ultrafine grained microstructure can be obtained through combining with hot rolling or other technologies [20,21], greatly improving the mechanical properties. However, to the best of our knowledge, little attention has been paid to the combining oxide dispersion-strengthening and martensitic microstructure refinement in maraging steels. It is widely acknowledged that lath martensite is a hierarchical microstructure. More specifically, one austenite grain is divided into martensitic packets (laths with the same habit plane) and every packet is further subdivided into martensitic blocks (laths with the same orientation), forming 24 variants in Kurdjumov-Sachs (K–S) relationship [22,23]. Morito et al. [24] studied the effect of PAGS on the morphology and crystallography in low carbon steels revealing that when the PAGS decreased to approximately 2 μm, a single packet tended to grow predominantly, with each packet consisting of blocks that contained sub-blocks. Nevertheless, the morphology and crystallography of lath martensite starting from submicron-sized austenite grain as yet is unknown. In this work, a novel oxide-dispersed maraging steel with ultrafine-grained microstructure was prepared by high-energy ball milling, and its martensite transformation behavior, morphology and crystallography of martensite and tensile properties were studied and compared the properties of its oxide-free counterpart.

2. Experimental procedures

In this study, T250 maraging steel was prepared by vacuum induction melting and vacuum arc remelting. The obtained ingot with a weight of 15 kg was homogenized at 1250 °C for 48 h, subsequently forged into rods with diameter of 60 mm, followed by air cooling. Moreover, for comparison, pre-alloyed metal powders of T250 maraging steel were prepared using the gas-atomization technology, and the diameter of metal powder particles was controlled to be less than 75 μm through sieving. Subsequently, 0.5 wt% Y_2O_3 powders (30–50 nm in diameter) were mixed with the pre-alloyed metal powders and then introduced into a milling chamber. The mass ratio of balls to powders was 10:1, and the rotational speed of ball milling was set to 250 rpm. Both the milling chamber and the balls were made of 304 stainless steels. After ball milling in a high-purity Ar gas atmosphere for 90 h, the powders were packed into a 304 stainless steel can and sealed under 10^{-4} Pa at 400 °C. Afterwards, the canned powders were consolidated by hot isostatic pressing in Ar pressure of 150 MPa at 1150 °C for 4 h. The consolidated sample was forged into a square blank about 40 mm on a side at 1150 °C, and subsequently hot rolled into plates with a thickness of about 15 mm at 1150 °C. In this work, the T250 maraging steel without Y_2O_3 powders was labeled as T250, while its counterpart with Y_2O_3 powders was labeled as ODS-T250. Table 1 shows the chemical compositions of the ODS-T250 and T250 steels. The specimens from the ODS-T250 and T250 steels were solid-solution treated at 800 °C, 1000 °C, and 1200 °C for 1 h, respectively, followed by water quenching.

For the characterization of martensite transformation behavior, thermal expansion experiments were performed using a thermo-mechanical analyzer DIL821 dilatometer. The diameter and length of samples was 5 mm and 20 mm, respectively. Samples were heated from room temperature to 800 °C at a rate of 0.05 °C/s, and then cooled to room temperature at a rate of 30 °C/s. Dog-bone shaped tensile samples with a gage length of 35 mm, a thickness of 1.5 mm, and a width of 14 mm were cut by electrical-discharge machining, and room temperature tensile tests were conducted on a MTS810 testing machine with a strain rate of 1×10^{-4} s^{-1}. The fracture morphology of tensile samples was observed using FEI XL-30 field-emission scanning electron microscope (FE-SEM).

Samples for electron backscatter diffraction (EBSD) measurements and X-ray diffraction (XRD) tests were mechanically polished and then electropolished in an electrolyte (10 vol% perchloric acid and 90 vol% ethanol) for 130 s with a current of 0.1 A and at −27 °C. EBSD measurements were performed using a FEI XL-30 field-emission SEM equipped with an EBSD detector to examine the morphology and crystallography of lath martensite. The acceleration voltage was 20 kV, and the step sizes for the ODS-T250 and T250 samples were 0.015 μm and 0.25 μm, respectively. EBSD raw data were processed by HKL Channel 5 software, and crystallographic analysis was performed using the MTEX (5.11.2)and ORTools(2.3.0) computer programs [25]. To examine the existence of retained austenite, XRD tests were conducted by a Bruker AXS D8 Advance X-ray monochromator with Cu Kα radiation at a scanning rate of 1.0°/min in the 2θ range of 40–140°. The dislocation density was calculated using a convolutional multiple whole profile (CMWP) computer program [26,27]. Foils for high-resolution transmission electron microscope (HR-TEM) characterization were mechanically polished to a thickness of 50 μm using SiC papers, and then punched into discs with a diameter of 3 mm. These discs were further thinned by twin-jet polishing to electron transparency using a 10 vol% perchloric acid solution at −27 °C. Energy dispersive X-ray spectroscopy (EDS) measurements and selected area electron diffraction (SAED) analysis were performed on a FEI Talos F200i TEM operated at 200 kV. For precipitates with regular shapes, the size was determined by an area equivalent diameter ($d = 2\sqrt{S_{Area}/\pi}$); for those of irregular shapes, an effective particle diameter, d_c, was defined as $d_c = \sqrt{d_1 d_2}$, where d_1 and d_2 are the smallest and largest dimensions, respectively. The average precipitate size, d_a, was calculated according to precipitate size distributions [28]. The volume fraction of nano-precipitates $f = 4/3\pi(d_a/2)^3 N_V$ was calculated by multiplying the particle number density with the average volume. The number density N_V was evaluated by $N_V = N_A/d_a$, where N_A represents the area density of precipitates. For each specimen, at least 5 TEM images containing above 200 particles were measured to obtain d_a, f, and N_V [29,30].

Table 1
Chemical compositions of the ODS-T250 and T250 steels (in wt.%).

	C	P	S	Ni	Mo	Ti	Y	O
ODS-T250	0.01	<0.005	0.007	18.42	3.00	1.69	0.40	0.26
T250	<0.01	<0.005	<0.003	18.85	2.97	1.35	–	0.003

3. Results

3.1. Microstructure characteristics

Fig. 1(a1, b1, c1), presents the inverse pole figure (IPF) coloring orientation map of as-quenched microstructure in the T250 steels after the solid solution treatment at 800, 1000 and 1200 °C, respectively. The as-quenched microstructure in the T250 steel is known to be lath martensite with hierarchical substructures [23,31–33]. Prior austenite grains are divided into several martensite packets with varying crystallographic orientations, and several martensite blocks are formed within each packet. These blocks are further subdivided into sub-blocks, and sub-blocks are again composed of martensite laths. It is universally claimed that the prior austenite grain boundaries, packet boundaries and block boundaries are classed as high angle grain boundaries (HAGBs), while the boundaries of sub-blocks and laths are grouped into low angle grain boundaries (LAGBs). In the current work, grain boundaries with misorientation angles between 15° and 45°are classified as prior austenite grain boundaries, based on previous work of Long et al. [34]. As shown in Fig. 1(a2, b2, c2), the green, blue and red lines correspond to grain boundaries with the misorientation angle range of $2° \leq \theta < 15°$, $15° \leq \theta \leq 45°$ and $45° < \theta$, respectively. As the solid solution temperature increases, the proportion of LAGBs rises from 60.0 % to 74.4 %, while that of PAGBs decreases from 6.6 % to 1.8 %. Additionally, the proportion of block and packet boundaries decreases from 34.4 % to 23.8 %. It is well recognized that HAGBs, typically defined by a misorientation angle equals to or greater than 15°, can effectively impede or arrest the propagation of microcracks [35]. In this study, a misorientation threshold of 15° was used as the criterion for identifying HAGBs, and the equivalent circular diameters of grains delineated by these boundaries were measured to determine the effective grain size. As shown in Fig. 1(a3, b3, c3), the effective grain size was calculated and found to increase with the solid solution temperature, reaching values of 3.446, 4.483 and 5.473 μm, respectively.

Fig. 2(a1, b1, c1), presents the inverse pole figure (IPF) coloring orientation map of as-quenched microstructure in the ODS-T250 steels after the solid solution treatment at 800, 1000 and 1200 °C, respectively. Notably, the martensitic morphology exhibits significant changes, characterized by sub-micron equiaxial grains without an obvious orientation relationship between them, and it seemed that there were no obvious martensite substructures in the prior austenite grains. As shown in Fig. 2(a2, b2, c2), with increasing solid solution temperature, the proportion of LAGBs rises from 26.4 % to 29.3 %, the proportion of PAGBs decreases from 25.6 % to 19.9 %, and the proportion of block and packet boundaries increases from 48.0 % to 50.8 %. The effective grain size of ODS-T250 is shown in Fig. 2(a3, b3, c3). As the solid solution temperature increases, the effective grain sizes are 0.272, 0.279 and 0.348 μm, respectively. Due to the grain boundary pinning by the oxide particles, the PAGS of the ODS-T250 steel remains essentially unchanged even when quenched from 1200 °C.

Quantitative phase analysis using EBSD revealed that both T250 and ODS-T250 steels exhibited a full martensite microstructure after quenching. Additionally, XRD measurements confirmed the absence of retained austenite in the as-quenched martensite for both steels, irrespective of the solid-solution temperature, as shown in Fig. 3(a). Moreover, a case of CMWP fitting profile from the sample quenched from 800 °C is also shown in Fig. 3(b), and it can be seen that the difference between the measured profile and the CMWP fitting profile is relatively small. The measured dislocation densities of the T250 and ODS-T250 steels are $2.87 \times 10^{15}/m^2$ and $2.68 \times 10^{15}/m^2$, respectively.

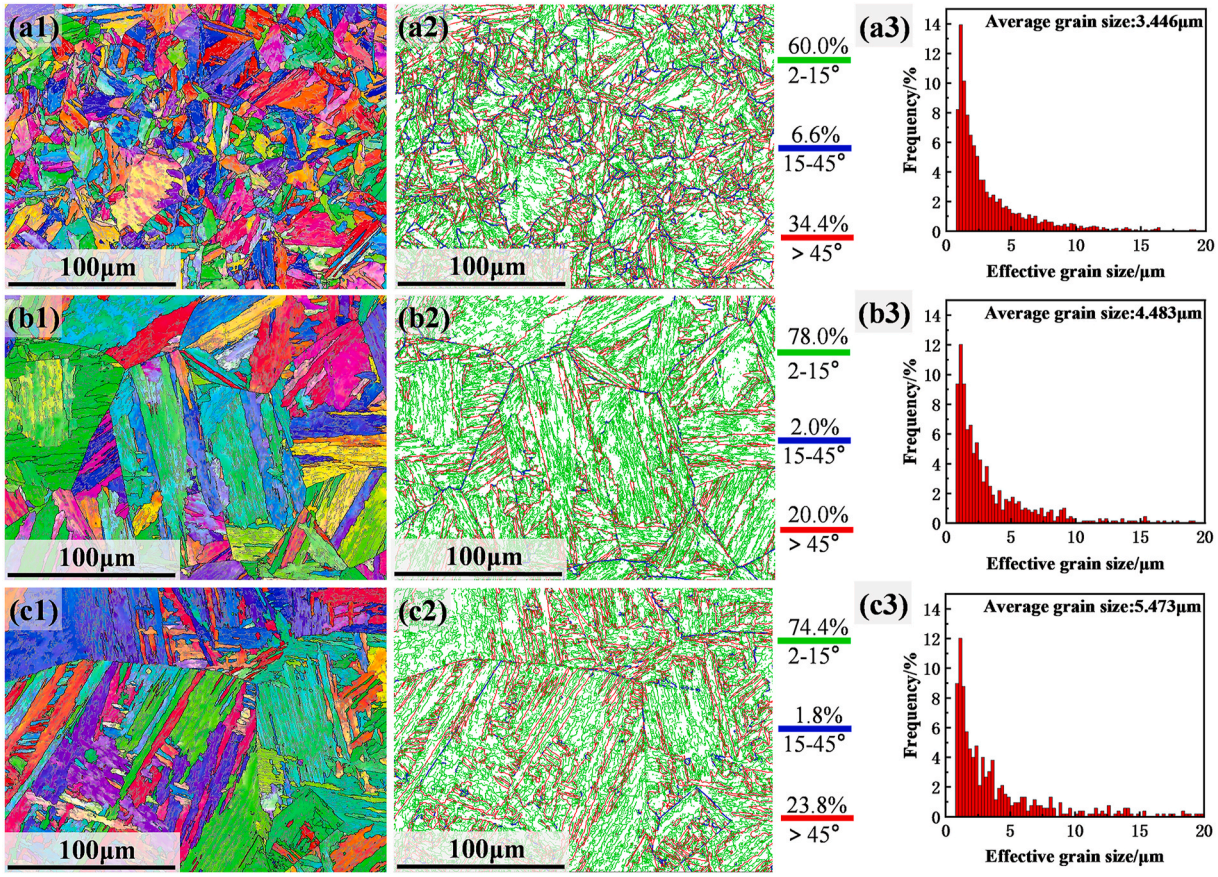

Fig. 1. IPF orientation maps (a1, b1, c1), grain boundary characteristics and distribution (a2, b2, c2), and effective grain size (a3, b3, c3) of T250 steel quenched from 800 °C (a1-a3), 1000 °C (b1-b3), and 1200 °C (c1-c3), respectively.

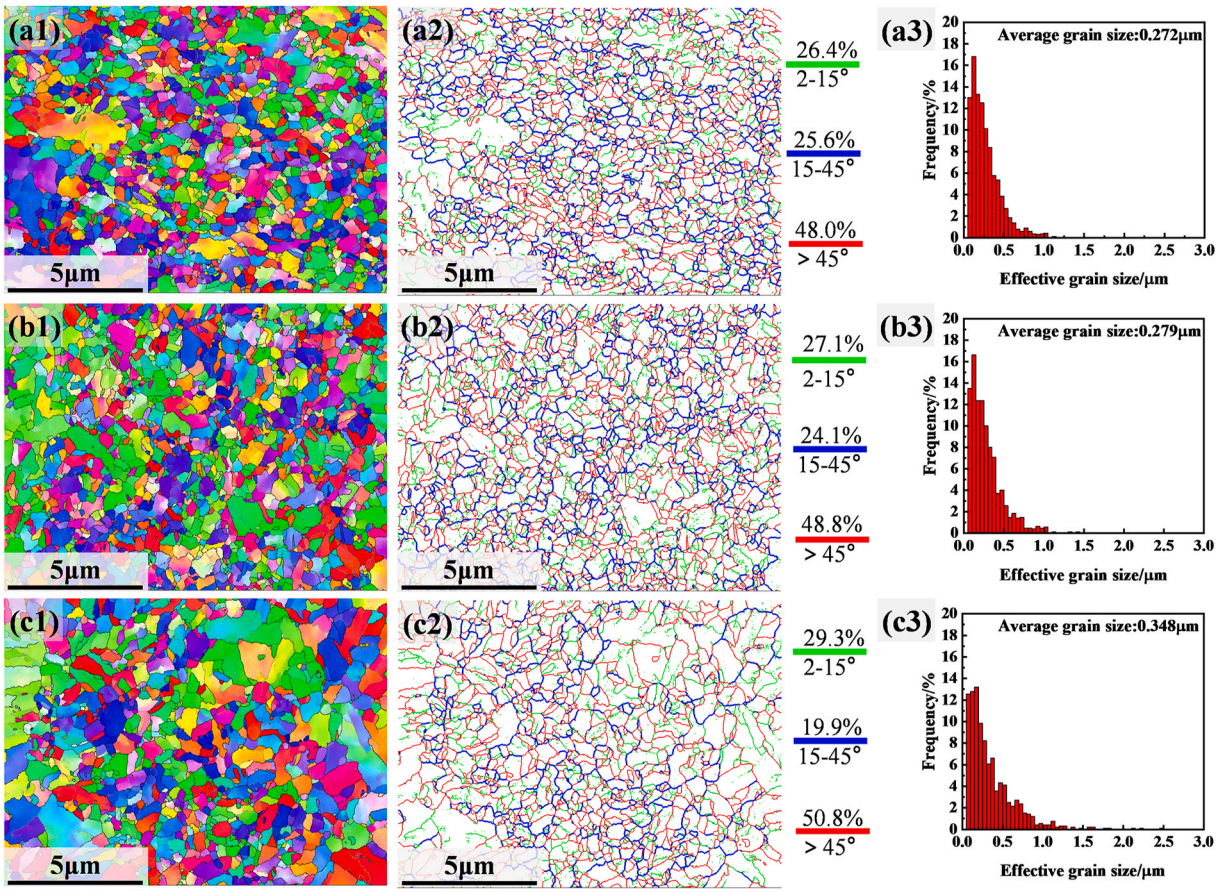

Fig. 2. IPF orientation maps (a1, b1, c1), grain boundary characteristics and distribution (a2, b2, c2), and effective grain size (a3, b3, c3) of ODS-T250 steel quenched from 800 °C (a1-a3), 1000 °C (b1-b3), and 1200 °C (c1-c3), respectively (note the reduction in grain size values with respect to Fig. 1).

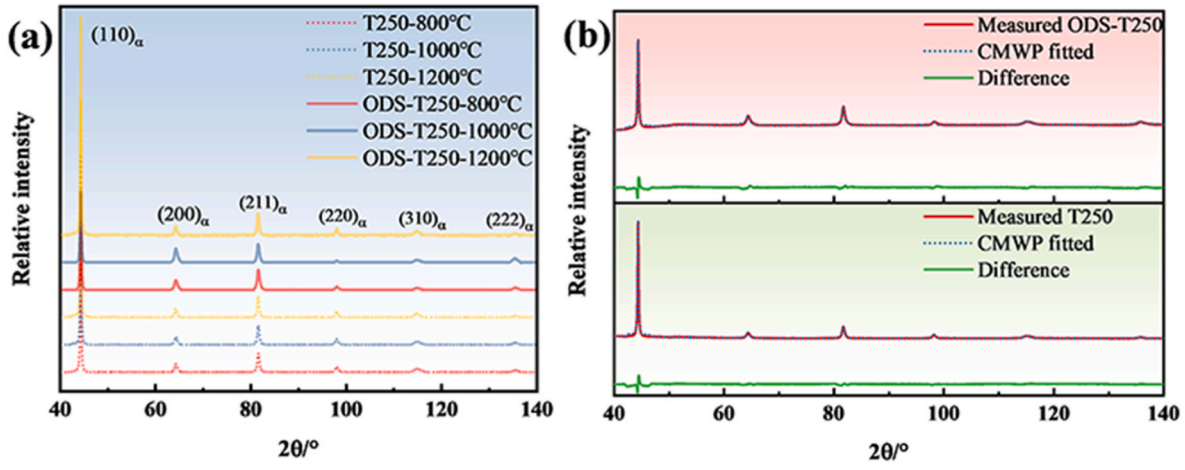

Fig. 3. XRD line profiles of the T250 and ODS-T250 steels quenched from various solid-solution temperatures (a), CMWP fitted XRD profile of T250 and ODS-T250 quenched from 800 °C (b).

To further investigate the microstructure characteristics of ODS-T250 steel after different solid solution treatments, transmission electron microscopy (TEM) analysis was conducted to examine martensite sub-grain morphology and oxide particle distribution. As shown in Fig. 4 (a–c), martensitic sub-grains exhibited equiaxed morphologies after quenching from 800, 1000, and 1200 °C. Interestingly, further observations indicated there was no martensitic laths in the as-quenched ODS-T250 steel, as shown in Fig. 4(d–f). Moreover, the growth of prior austenite grains remained constrained despite increasing quenching temperature. Nano-sized spherical oxides were uniformly dispersed in the martensitic matrix, and some of them (indicated by the red arrows) were situated at prior austenite grain boundaries. Moreover, as the solid-solution temperature increased, both the size and the volume fraction of spherical oxides increased, while their number density decreased, as shown in Table 2.

The type and crystal structure of the dispersed oxides were subsequently analyzed and identified. Fig. 5(a) is a high-angle annular dark-field scanning transmission electron microscopy (HAADF-STEM) image

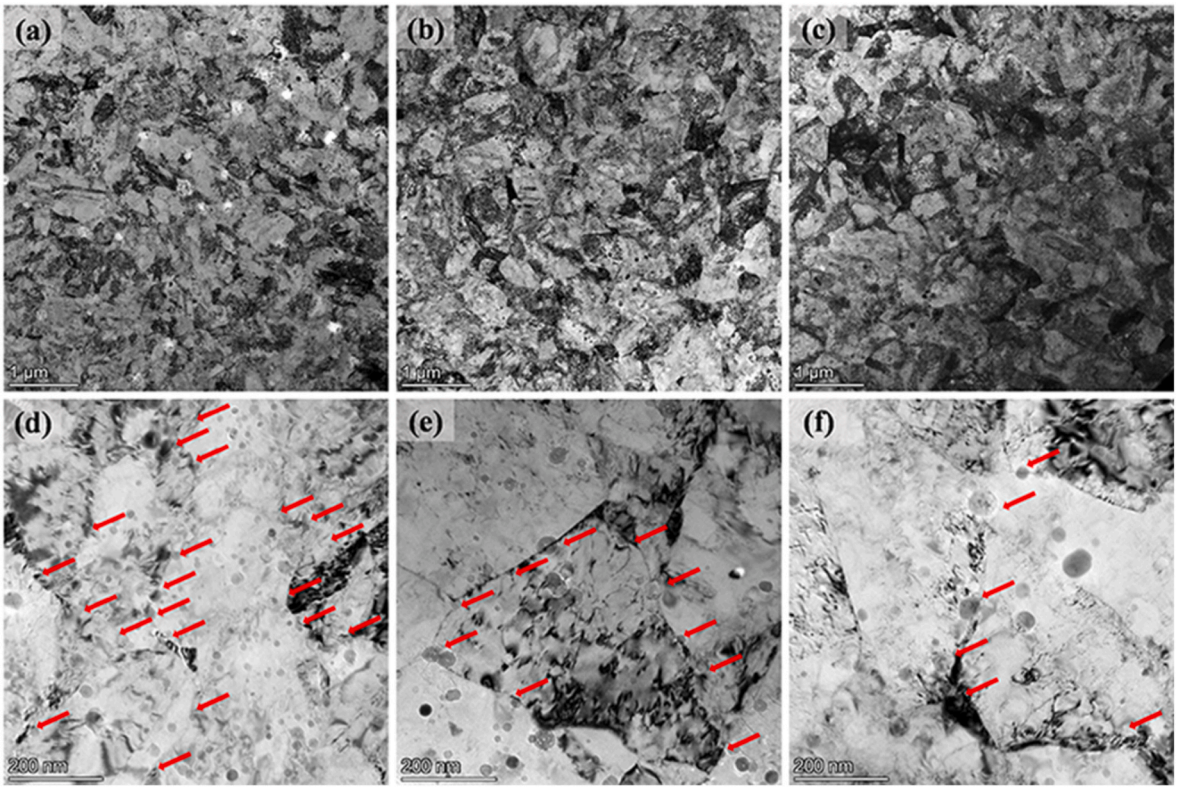

Fig. 4. TEM images showing the (a–c) equiaxed martensite sub-grains and (d–f) spherical oxides in ODS-T250 quenched from 800 °C (a–d), 1000 °C (b–e), and 1200 °C (c–f), respectively.

Table 2
The size, volume fraction and number density of spherical oxides in ODS-T250 steel after various solid-solution treatments.

Solid solution temperature/ °C	Size/ nm	Number density/ m^{-3}	Volume fraction
800	12.7	9.2×10^{21}	0.0099
1000	14.4	6.6×10^{21}	0.0102
1200	21.4	4.4×10^{21}	0.0226

from the as-quenched ODS-T250 steel after the solid-solution treatment at 800 °C. Based on elemental distribution analysis by EDS (Fig. 5(b–d)), it was found that a large number of nano-particles, enriched in Y, Ti, and O were dispersed in the martensite matrix. Fig. 5(e, f) are the HR-TEM images of selected particles, and the atomic fractions of alloying elements for each selected particle based on EDS point analysis were attached. For the large particle as shown in Fig. 5(e), the corresponding fast Fourier transform (FFT) image identified this particle as hexagonal-Y_2TiO_5 [36], which had lattice parameters of $a = b = 3.608$ Å, $c = 10.6056$ Å and $\alpha = \beta = 90°$, $\gamma = 120°$. The zone axis of this particle was $[\bar{5}11]$, with adjacent atomic planes of $(01\bar{1})$ and $(\bar{1}0\bar{5})$. For the fine particle as shown in Fig. 5(f), it was identified as FCC-$Y_2Ti_2O_7$ [37] with lattice parameters of $a = b = c = 10.089$ Å and $\alpha = \beta = \gamma = 90°$. The zone axis of this particle was [101], with adjacent atomic planes of $(1\bar{1}\bar{1})$ and $(\bar{2}02)$. The corresponding inter-planar spacings were 5.83 Å and 3.75 Å, respectively, with an angle of 35°.

3.2. Reconstruction of parent austenite and crystallography of individual grains

It has been well acknowledged that martensitic transformation is characterized by a strict orientation relationship between the martensite and the parent austenite. Although there are Kurdjumov-Sachs (K–S) [38], Nishiyama-Wasserman (N–W) [39,40], and Greninger-Troiano (G-T) [41] orientation relationships related to the martensitic transformation in steels, the martensite transformation in T250 maraging steel was reported to strictly follow the K–S orientation relationship [42,43]. Specifically, the K–S orientation relationship is characterized by {111}γ//{110}α and <110>γ//<111>α. Table 3 summarizes the positional relationships of these 24 martensite variants based on the compound K–S orientation relationship [44]. According to the K–S orientation relationship, these 24 martensite variants could be divided into 4 close-packed (CP) groups based on close-packed parallel planes including CP1: (111) γ// (011) α, CP2: $(1\bar{1}1)$ γ// (011) α, CP3: $(\bar{1}11)$ γ// (011) α and CP4: $(11\bar{1})$ γ// (011) α. Every CP group (Packet) was further composed of 6 close-packed plane variants with similar K–S orientation relationship between them. Moreover, these 24 martensite variants could also be divided into 3 Bain groups, and the 8 variants in every group enjoyed similar crystal structures, namely B1: [001] γ// [001] α, B2: [100] γ// [110] α, and B3: [010] γ// $[\bar{1}10]$ α [23,32,45,46].

The prior austenite grains in T250 steel were reconstructed based on the K–S relationship [38]. Fig. 6 illustrates the distribution of the 24 martensite variants after quenching from 800, 1000 and 1200 °C. As shown in Fig. 6(a–c), each variant is represented by unique color, revealing that each prior austenite grain contains multiple variants. This color difference indicated that the variant selection during martensite transformation varied from one prior austenite grain to another. The relative frequency of the martensite variants is shown in Fig. 6(d–f). The as-quenched T250 steel exhibited 24 variants after different solid solution treatments, with varying proportions among them, some being more prevalent than others. When the T250 steel was quenched from 800 °C, the proportions of V5, V6, V19, V22 and V23 were 5.6 %, 4.9 %, 5.9 %, 7.7 % and 5.1 %, respectively, which were slightly higher than the average value. The proportions of other martensite variants were nearly uniform. When the T250 steel was quenched from 1000 °C, the proportions of V3, V6, V9, V13, V15, V16 and V18 were 7.1 %, 5.5 %,

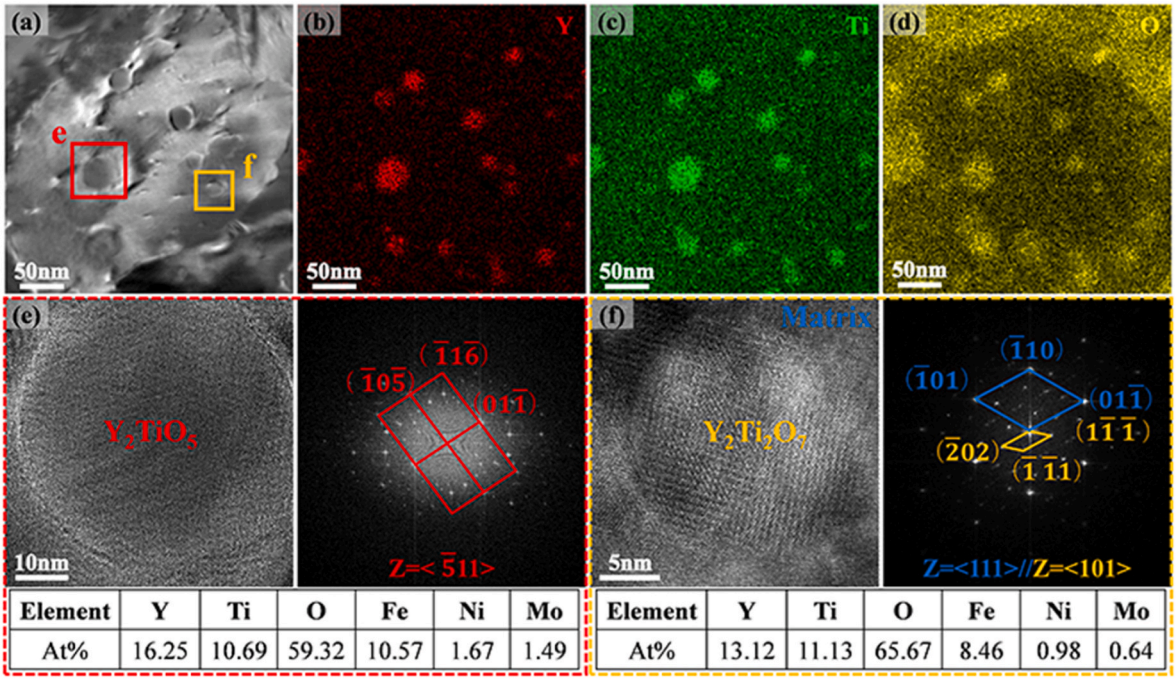

Element	Y	Ti	O	Fe	Ni	Mo
At%	16.25	10.69	59.32	10.57	1.67	1.49

Element	Y	Ti	O	Fe	Ni	Mo
At%	13.12	11.13	65.67	8.46	0.98	0.64

Fig. 5. TEM images of spherical oxides in ODS-T250 steel quenched from 800 °C. (a) HAADF-STEM image, (b–d) EDS-mapping images of Y, Ti and O, (e) HR-TEM image corresponding to Y_2TiO_5 (f) HR-TEM image corresponding to $Y_2Ti_2O_7$.

6.9 %, 6.9 %, 7.8 %, 7.1 % and 6.7 %, respectively. In contrast, the proportions of V8, V11 and V17 were 1.4 %, 1.7 % and 2.1 %, respectively. Moreover, when the T250 steel was quenched from 1200 °C, the proportions of V2, V8, V11, V17 and V21 were 10 %, 8.1 %, 11.4 %, 6.3 % and 7.0 %, respectively, while V1, V4 and V13 had relatively low proportions (about 1.5 %). As the solid solution temperature increased, prior austenite grains grew, and certain martensite variants exhibited preferential formation.

To analyze the crystallography of individual prior austenite grains in T250 steel quenched from 800 °C, two representative grains (Grain A and Grain B) were selected and reconstructed. As shown in Fig. 7, the distribution of martensitic variants, CP group and Bain group are compared between grain A (Fig. 7(a)) and B (Fig. 7(b)). The 24 martensite variants are represented by different colors. As shown in Fig. 7(a2-a3) and (b2-b3), Bain1, Bain2, and Bain3 are highlighted in white, red, and black, respectively, while CP1-CP4 are marked in purple, blue, green and yellow, respectively. In grain A, the areas of V3, V6, V14, V20, and V21 accounted for 13.8 %, 7.6 %, 7.5 %, 12.7 % and 8.5 %, respectively. V7 was absent, and V2, V5, V10, V19 as well as V22 had very low proportions. But in grain B, V2, V10 and V18 prevailed, occupying 14.3 %, 23.7 % and 14.8 %, respectively. V13, V16 and V24 even did not appear in grain B, as shown in Fig. 7(c). In terms of the CP group, CP1 (33.6 %), CP3 (24.7 %) and CP4 (31.1 %) were popular in grain A, while CP2 (52.1 %) dominated in grain B (Fig. 7(d)). As for the Bain group, Bain1 (40.9 %) was about two times larger than Bain2 (22.8 %) for grain A. Bain2 (68.4 %) was much larger than the other two Bain groups in grain B (Fig. 7(e)). It could be seen in Fig. 10 that each CP group included at most 6 variants, while each Bain group consisted of either a single variant or variants with low misorientation. Each CP group contained only two or three Bain groups which were arranged in a staggered way. The misorientation between the Bain groups was significant, resulting in HAGBs in the CP group. Compared to grains A and B, both grains contained multiple variants, although not all 24 variants were present in each grain. As a result, the selection of different variants led to distinct CP and Bain group distributions in the two grains.

In the ODS-T250 steel, as shown in Fig. 8(a–c), 24 martensite variants again are represented by different colors. For the ODS-T250 steel quenching from 800 °C, most of prior austenite grains contain a single variant, with only a few slightly larger grains containing multiple variants. As the PAGS increased, the number of prior austenite grains containing two or more variants also increased. Fig. 8(d–f) shows the statistical distribution of martensite variants in ODS-T250 steel after various solid-solution temperatures. More specifically, after quenching from 800 °C, the proportions of V1, V6, V8 and V23 were 5.0 %, 5.2 %, 6.5 % and 5.2 %, respectively, which were slightly higher than the average value. After quenching from 1000 °C, the proportions of variants V11, V13, and V22 were 5.5 %, 7.1 %, and 6.5 %, respectively, while the proportion of V16 was only 2.3 %. And after quenching from 1200 °C, V4, V19 and V24 enjoyed higher proportions, accounting for 8.6 %, 8.7 % and 6.6 %, respectively.

Reconstructed grains from the specimen quenched at 800 °C in ODS-T250 were selected, and labeled Grain C and Grain D. The distribution of martensitic variants, CP groups, and Bain groups in grains C and D are shown in Fig. 9. In grain C, V10, V11, V18 and V22 accounted for 0.3 %,7.7 %, 18.2 % and 73.8 %, respectively. For CP group, grain C was composed of CP2, CP3 and CP4, which accounted for 8.0 %,18.2 % and 73.8 %, respectively. The habit plane for grain C was primarily the $(11\bar{1})_\gamma$ plane. Moreover, grain C contained Bain1, Bain2, and Bain3, accounting for 7.8 %, 18.4 % and 73.8 %, respectively. In contrast, grain D contained only a single variant, V20, and its habit plane is $(11\bar{1})_\gamma$. Likewise, grain D had only one CP group and one Bain group, CP4 and Bain2, respectively. These results highlight the variant reduction effect in the ultrafine-grained ODS-T250 steel, with a single variant existing in most grains, causing the formation of ultrafine equiaxed martensite.

To investigate the effect of PAGS on the number of variants in a prior austenite grain, 150 prior austenite grains from the ODS-T250 steel after quenched from 800 °C were randomly selected for statistical analysis, and the results are shown in Fig. 10. It was observed that as PAGS increased, the number of variants in each prior austenite grain also increased. Specifically, when the PAGS was decreased down to about 0.43 μm, only a single variant would form in a prior austenite grain. This indicated that the number of variants in a prior austenite grain is strongly influenced by PAGS.

Table 3
24 martensite variants in K–S orientation relationship.

Variant	Plane parallel	Direction parallel	Misorientation angle from V1 (°)	CP group	Bain group
V1	$(111)_\gamma$// $(011)_\alpha$	$[\bar{1}01]_\gamma$// $[\bar{1}\bar{1}1]_\alpha$	–	CP1	B1
V2		$[\bar{1}01]_\gamma$// $[\bar{1}1\bar{1}]_\alpha$	60.0		B2
V3		$[01\bar{1}]_\gamma$// $[\bar{1}\bar{1}1]_\alpha$	60.0		B3
V4		$[01\bar{1}]_\gamma$// $[\bar{1}1\bar{1}]_\alpha$	10.5		B1
V5		$[1\bar{1}0]_\gamma$// $[\bar{1}\bar{1}1]_\alpha$	60.0		B2
V6		$[1\bar{1}0]_\gamma$// $[\bar{1}1\bar{1}]_\alpha$	49.5		B3
V7	$(1\bar{1}1)_\gamma$// $(011)_\alpha$	$[10\bar{1}]_\gamma$// $[\bar{1}\bar{1}1]_\alpha$	49.5	CP2	B2
V8		$[10\bar{1}]_\gamma$// $[\bar{1}1\bar{1}]_\alpha$	10.5		B1
V9		$[\bar{1}\bar{1}0]_\gamma$// $[\bar{1}\bar{1}1]_\alpha$	50.5		B3
V10		$[\bar{1}\bar{1}0]_\gamma$// $[\bar{1}1\bar{1}]_\alpha$	50.5		B2
V11		$[011]_\gamma$// $[\bar{1}\bar{1}1]_\alpha$	14.9		B1
V12		$[011]_\gamma$// $[\bar{1}1\bar{1}]_\alpha$	57.2		B3
V13	$(\bar{1}11)_\gamma$// $(011)_\alpha$	$[0\bar{1}1]_\gamma$// $[\bar{1}\bar{1}1]_\alpha$	14.9	CP3	B1
V14		$[0\bar{1}1]_\gamma$// $[\bar{1}1\bar{1}]_\alpha$	50.5		B3
V15		$[\bar{1}0\bar{1}]_\gamma$// $[\bar{1}\bar{1}1]_\alpha$	57.2		B2
V16		$[\bar{1}0\bar{1}]_\gamma$// $[\bar{1}1\bar{1}]_\alpha$	20.6		B1
V17		$[110]_\gamma$// $[\bar{1}\bar{1}1]_\alpha$	51.7		B3
V18		$[110]_\gamma$// $[\bar{1}1\bar{1}]_\alpha$	47.1		B2
V19	$(11\bar{1})_\gamma$// $(011)_\alpha$	$[\bar{1}10]_\gamma$// $[\bar{1}\bar{1}1]_\alpha$	50.5	CP4	B3
V20		$[\bar{1}10]_\gamma$// $[\bar{1}1\bar{1}]_\alpha$	57.2		B2
V21		$[0\bar{1}\bar{1}]_\gamma$// $[\bar{1}\bar{1}1]_\alpha$	20.6		B1
V22		$[0\bar{1}\bar{1}]_\gamma$// $[\bar{1}1\bar{1}]_\alpha$	47.1		B3
V23		$[101]_\gamma$// $[\bar{1}\bar{1}1]_\alpha$	57.2		B2
V24		$[101]_\gamma$// $[\bar{1}1\bar{1}]_\alpha$	21.1		B1

3.3. Martensitic transformation behavior

Fig. 11(a) shows the thermal expansion curves of the T250 and ODS-T250 steels during heating and cooling, revealing critical phase transformation temperatures. The Ac1, Ac3, and Ms temperatures of the T250 steel were 567, 697 and 183 °C, respectively. In contrast, The Ac1, Ac3, and Ms temperatures of the ODS-T250 steel were 558, 662 and 92 °C, respectively. This indicated that under the same heating condition, the austenite transformation in ODS-T250 steel started and finished before that in T250 steel. However, the martensite transformation was postponed by 91 °C in ODS-T250 steel compared with T250 steel. Fig. 11(b) shows the change in martensite fraction in T250 and ODS-T250 steels during cooling. As shown in Fig. 11(b), the martensite fraction increased as the temperature decreased for both steels. Specifically, for T250 steel, martensite formed slowly in the initial stage, reaching 6 % when the temperature dropped 21 °C below its Ms temperature. Subsequently, during cooling to 130 °C, the fraction of martensite in the T250 steel rapidly increased to 50 %, followed by a slow transformation stage till the end of martensite transformation. By contrast, the ODS-T250 steel showed a faster martensite formation during the initial stage, reaching 6 % only when the temperature dropped just 10 °C below its Ms temperature. Subsequently, 50 % of the martensitic transformation occurred with a further temperature decrease of only 18 °C. In the following stage, martensite formation continued at a high rate until the transformation was completed.

3.4. Room temperature tensile properties and fractography

Fig. 12 shows the engineering stress-strain curves of the T250 and ODS-T250 steels after quenching from 800, 1000 and 1200 °C. As the solid-solution temperature increased, both the strength and elongation of the studied steels decreased. Interestingly, the strength of the ODS-T250 steel was much higher than that of the T250 steel irrespective of the solid-solution temperature. Moreover, compared with the T250 steel, no obvious degradation of ductility was found in the ODS-T250 steel with the increase in strength, and there was a certain degree of improvement in ductility of the ODS-T250 steel even after quenching from 800 to 1000 °C. Specifically, after quenching from 800 °C, the yield strength and tensile strength of ODS-T250 steel increased by 152 MPa and 258 MPa, respectively, compared to T250 steel. Moreover, the ductility of ODS-T250 was slightly superior to that of T250. When the solid-solution temperature was increased to 1000 °C, the yield strength (951 MPa), tensile strength (1161 MPa) and ductility (7.6 %) of the ODS-T250 steel were still higher than that of the T250 steel. After quenching from 1200 °C, both the tensile strength and yield strength of the ODS-T250 steel were higher than that of the T250 steel, while the ductility nearly remained unchanged.

To clarify the fracture mode of T250 and ODS-T250 steels after quenching from different solid-solution temperatures, we examined their tensile fracture morphologies. As shown in Fig. 13(a–c), the degree of necking decreased with the increase of solid-solution temperature. More specifically, for the T250 steel quenched from 800 °C, there were deeper dimples with varying sizes on the fracture surface (Fig. 13(a)), indicating that the fracture took place in a ductile mode. Moreover, although the T250 steel quenched from 1000 °C fractured with necking failure and dimples with various sizes could be found, its fracture was thought to be quasi-cleavage mode due to river patterns (Fig. 13(b)). As for the T250 steel quenched from 1200 °C, however, a small number of shallow dimples and many river patterns could be found on the fracture surface and the percentage of the cleavage region increased (Fig. 13(c)), suggesting a quasi-cleavage fracture. For the ODS-T250 steel, the fracture morphologies of tensile samples quenched from 800 °C to 1000 °C were similar, as shown in Fig. 13(d and e), displaying some necking characteristics. A closer observation showed equiaxed dimples with different sizes and a few cleavage facets (cleavage steps river pattern). Decohesion by cleavage in grains could be also detected. The coexistence of cleavage facets and dimples indicated a mixed ductile and brittle fracture. However, when quenching from 1200 °C, there was almost no necking as shown in Fig. 13(f). The fracture surface was distributed with a large number of small and shallow dimples, and decohesion of grain boundaries was more evident, indicative of a reduced ductility.

4. Discussion

4.1. Effect of grain refinement on martensite variant in ODS-T250 steel

As shown in Fig. 4, the addition of Y_2O_3 powders and subsequent ball milling induced an ultrafine martensitic microstructure in ODS-T250 steel, even after quenching from 1200 °C. This was primarily

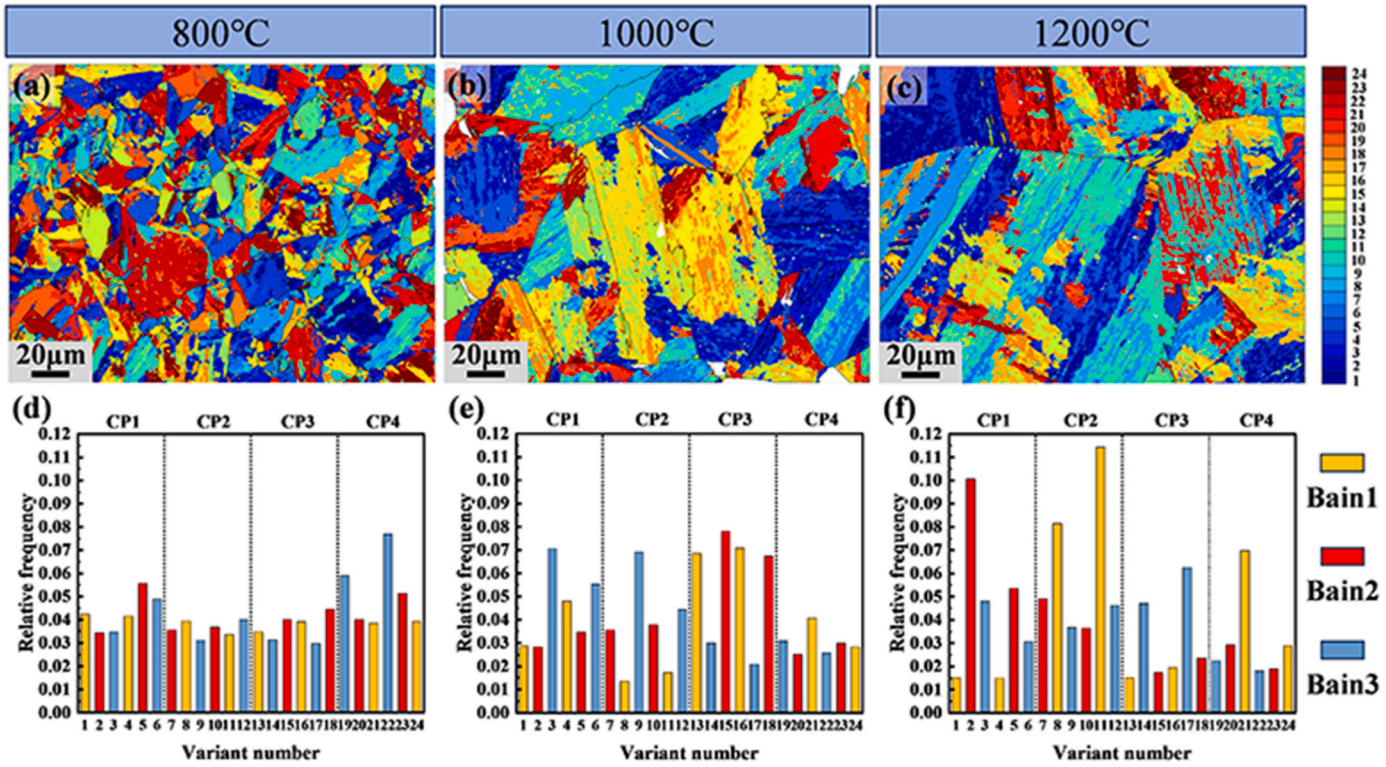

Fig. 6. (a–c) The distribution and (d–f) relative frequency of martensite variants in T250 steel quenched from (a, d) 800 °C, (b, e) 1000 °C and (c, f) 1200 °C, respectively.

attributed to the significant refinement of prior austenite grains. The oxides dispersed in matrix identified as Y_2TiO_5 and $Y_2Ti_2O_7$ exhibited excellent thermal stability, and the particles sizes only increased slightly with quenching temperature, as shown in Table 2. During the solution treatment, austenite grains tended to grow due to thermal activation. When their boundaries encountered these oxides, the growth of these austenite grains was possibly forced to stop, which may explain why nanosized oxides were predominantly located at prior austenite grain boundaries. Then, the particle-limited radius R_p of matrix grains can be calculated using Naila's formula [47], as shown in Eq. (1):

$$R_p = 3\pi r / 4f^{0.5} \quad (1)$$

where R_p is the particle-limited grain radius, r and f are the mean radius and the volume fraction of second-phase particles, respectively. The calculated values of R_p of the ODS-T250 steel after quenching from 800, 1000 and 1200 °C were 151, 167 and 168 nm, respectively. After converting these values to grain diameters, we found that the calculated particle-limited grain diameter closely corresponded to the effective grain size measured by EBSD. The stability of oxides and their pinning effect at grain boundaries enabled the formation of ultrafine-grained martensite with good thermal stability.

Compared to the martensite sub-grain morphology observed in T250 steel, the martensite in ODS-T250 steel exhibited an equiaxed morphology rather than a lath morphology. Further analysis of reconstructed grains revealed that most variants were present in a prior austenite grain of T250 steel, whereas only a few variants or even a single variant formed in a prior austenite grain of ODS-T250 steel, as shown in Figs. 7 and 9. The crystallographic anisotropy from parent austenite grains induced the difference in martensite variant selection among parent austenite grains. Moreover, the preferential alignment of martensitic variants adhered to the K–S orientation relationship at the austenite-martensite interface, thereby minimizing interfacial strain energy and volumetric distortion [48,49]. As demonstrated in the study, the PAGS exerted a strong influence on the formation and distribution of martensitic variants. In smaller PAGS, the elastic strain energy predominantly concentrated along the longitudinal direction of martensitic laths. This directional strain energy distribution suppressed the formation of multi-orientation variants, resulting in the predominant growth of a single dominant variant through repeated nucleation of parallel laths [50]. Morito et al. [24] also found that when the prior austenite grains were refined to 2 μm, a main packet formed within a prior austenite grain, with each packet containing blocks that were further subdivided into sub-blocks. In the current work, our results confirmed that when the PAGS was further decreased to the submicron-sized level, a prior austenite grain could only produce one martensitic variant. As shown in Fig. 10, our results confirmed that the critical PAGS size for single variant martensite formation is 0.43 μm. Clearly, ultrafine grains limit the variant selection during the martensitic transformation, leading to the formation of a single variant martensite, which appears as an equiaxed martensite without lath features.

4.2. Martensitic transformation behavior in ODS-T250 steel

Based on the thermal expansion curves of the T250 and ODS-T250 steels (Fig. 11(a)), the Ms temperature in the T250 steel (183 °C) was higher than in the ODS-T250 steel (92 °C). In particular, martensite formed with a rapider rate in the ODS-T250 steel during the initial stage, followed by a short stagnation. After that, the martensite transformation continued to occur when the temperature further decreased by 18 °C as shown in Fig. 11(b). As shown in Fig. 4, the as-quenched ODS-T250 steel featured not only submicron-sized ultrafine prior austenite grains but also high-density nano-sized oxides dispersed within the martensite matrix. Yin et al. [51] argued that the PAGS refinement increased the area of grain boundaries, which accelerated the transformation rate and induced fine martensitic laths. Hanamura et al. [52] observed that decreasing PAGS from 254 μm to 30 μm resulted in a decrease of 40 K in Ms temperature. Furthermore, Brofman and Ansell [53] claimed that the incorporation of Y_2O_3 particles up to 1.5 wt% into Fe–27Ni-0.025C

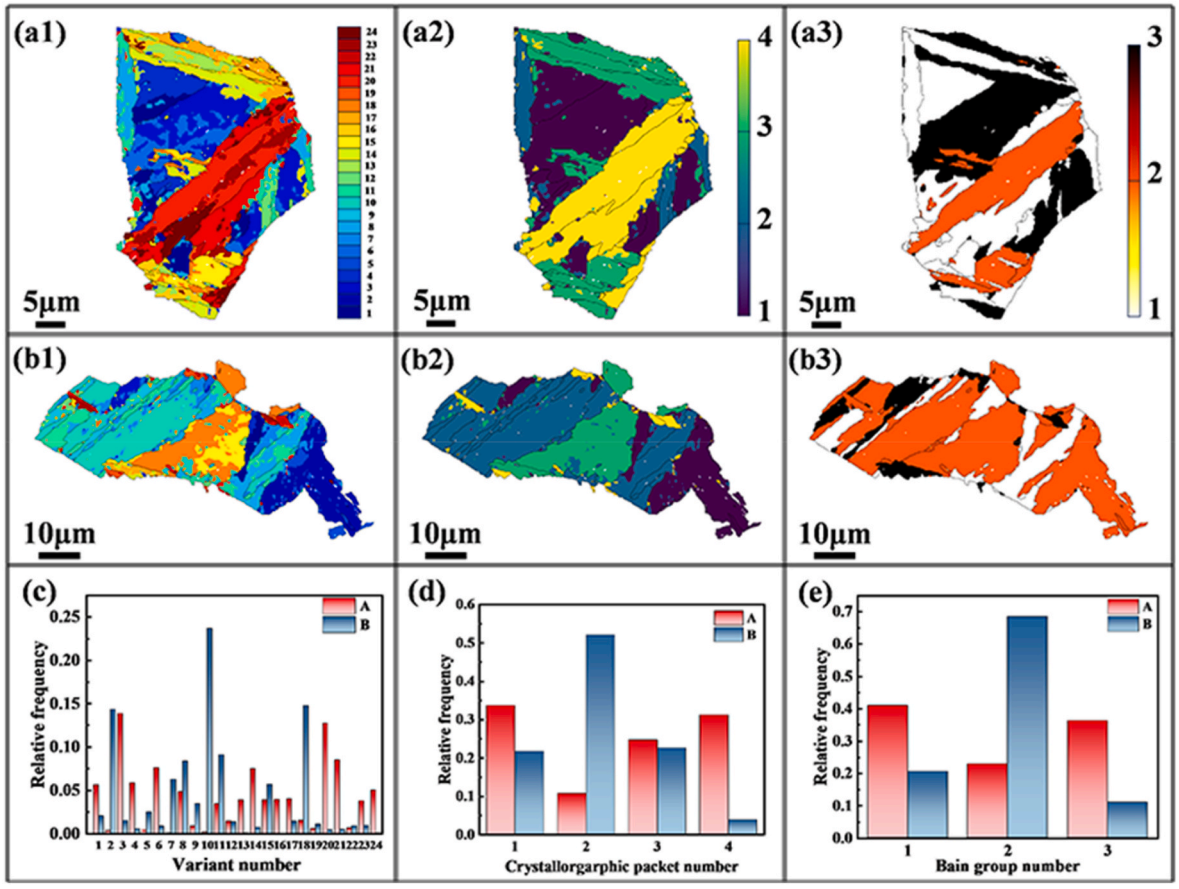

Fig. 7. (a1, b1) Martensite variants distribution, (a2, b2) CP groups distribution and (a3, b3) Bain groups distribution in grains (a) A and (b) B, the fraction of (c) 24 variants, (d) CP groups and (e) Bain groups.

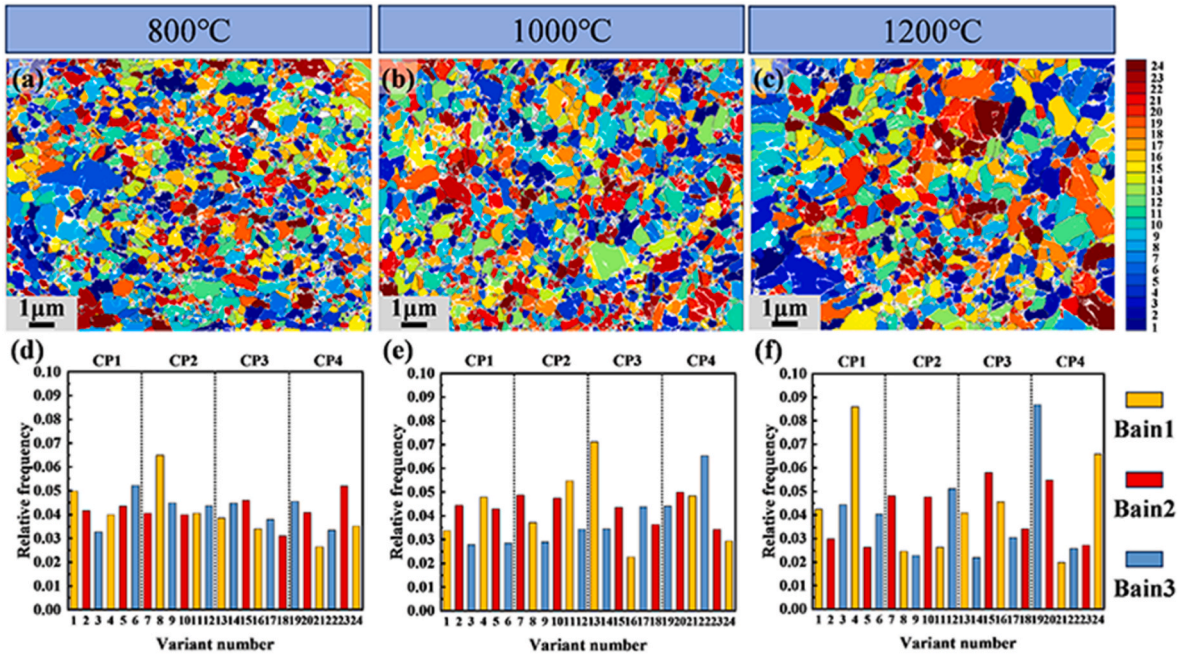

Fig. 8. (a–c) The distribution and (d–f) relative frequency of martensite variants in ODS-T250 steel quenched from (a, d) 800 °C, (b, e) 1000 °C and (c, f) 1200 °C, respectively.

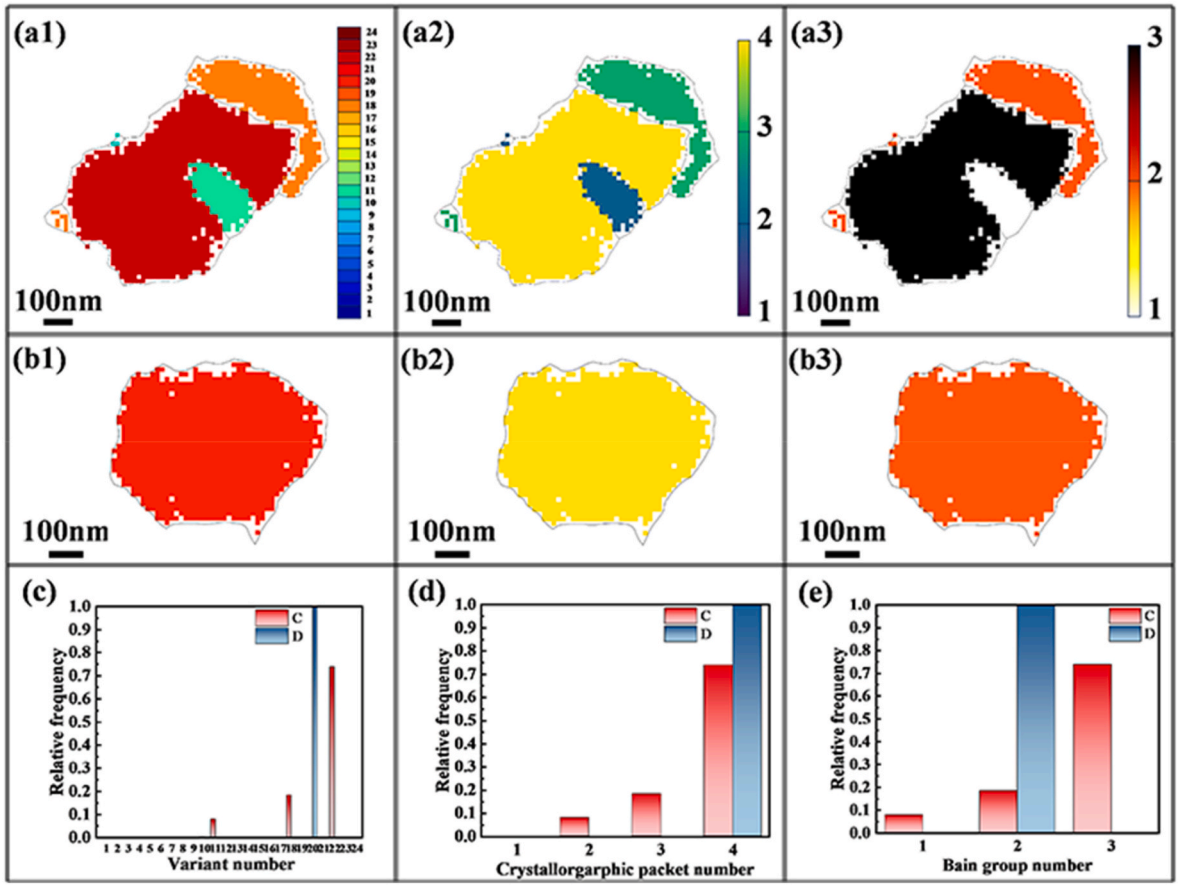

Fig. 9. (a1, b1) Martensite variants distribution, (a2, b2) CP groups distribution and (a3, b3) Bain groups distribution in grains (a) C and (b) D, the fraction of (c) 24 variants, (d) CP groups and (e) Bain groups.

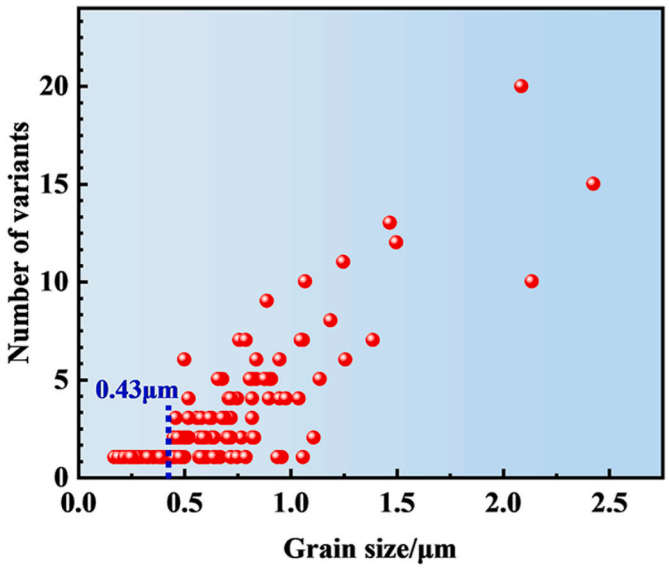

Fig. 10. The corresponding statistical data of PAGS vs. Number of variants for ODS-T250 material quenched from 800 C.

alloys induced a great decrease (39 °C) in Ms temperature. This indicated that oxides also enhanced the resistance to martensitic transformation, leading to the decrease in Ms temperature. Therefore, it could be concluded that refined PAGS and oxides were the primary contributors to the reduction in the Ms temperature of the ODS-T250 steel.

To assess the relative influence of these two factors on the Ms temperature, effects of the alloy composition and prior austenite grain size were initially analyzed, followed by an evaluation on the influence of oxides. Generally, the Ms temperature is decreased with an increase in solute concentration for most alloying elements except for Co [41] and Al [54]. Several studies have shown that decreasing the austenite grain size into the <10 μm level resulted in a decrease of Ms temperature [55–59]. After taking both alloy composition and PAGS into account, Lee and Park [60] proposed an empirical equation for calculating Ms temperature, as shown in Eq. (2):

$$M_s = k_0 + \sum_i k_i x_i + k_{pags} \ln(d_r) \quad (2)$$

where k_0 is a constant obtained for the Ms temperature of pure iron (°C), k_i is the coefficient for the alloying element i (°C/wt%), x_i is the amount of alloying element i (wt%), k_{pags} is a parameter related to the PAGS effect, d_r is the average prior austenite grain diameter (μm). The values of k_0 and k_{pags} are 475.9 and 11.67, respectively. The coefficient k_i for each alloy element is shown in Table 4.

Based on Eq. (2), The Ms temperature of the T250 and ODS-T250 steels was determined to be 195 °C and 148 °C, respectively. The calculated Ms temperature was reduced by 55 °C due to the refined PAGS, while the effects of minor compositional variations were neglected. Calculations also showed that the Ms temperature of the T250 steel was approximately 12 °C higher than the measured Ms temperature. Thus, it is estimated that those dispersed nano-sized oxides in the ODS-T250 steel decreased the Ms temperature by approximately 44 °C.

Martensite transformation is regarded as a shear-driven, coherent phase transformation, during which the crystal lattice reorganized through short-range migration of matrix atoms and the child phase

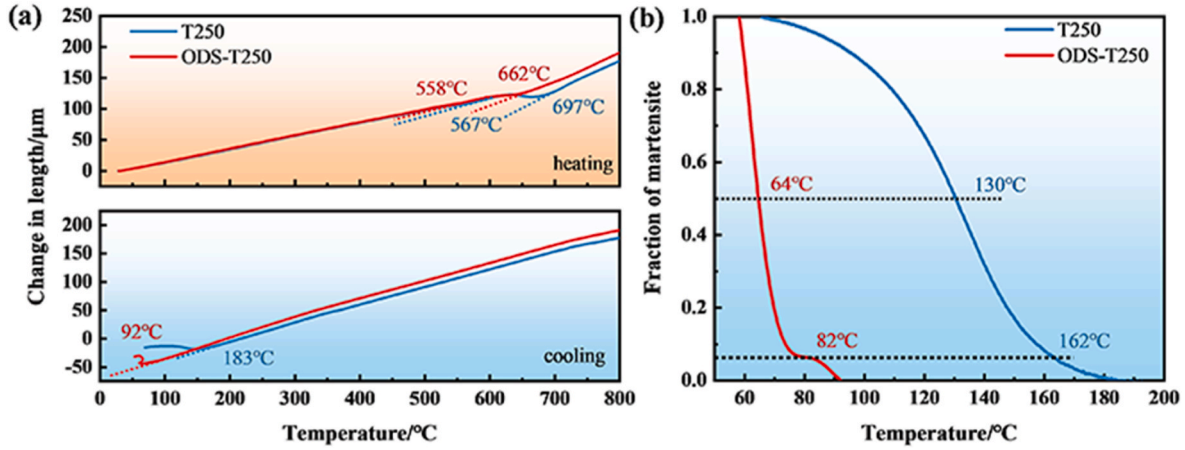

Fig. 11. (a) Thermal expansion curves and (b) the change in the fraction of martensite with cooling in T250 and ODS-T250 steels.

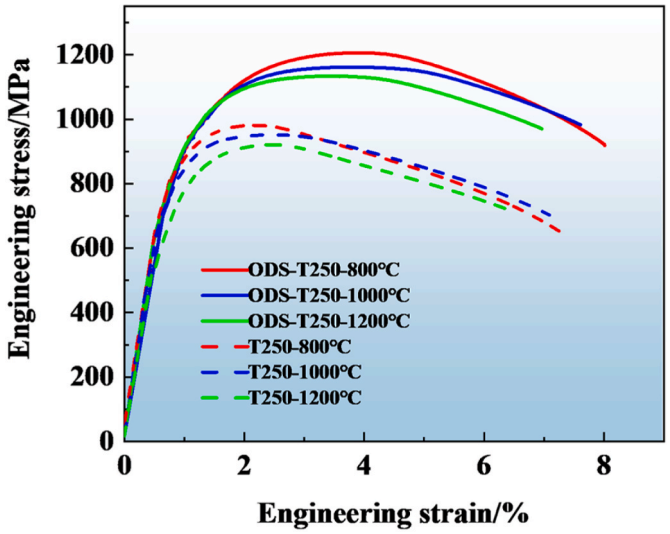

Fig. 12. Engineering stress-strain curves of T250 and ODS-T250 steels quenched from 800 °C, 1000 °C, and 1200 °C.

maintained coherent with the parent phase. The large number of oxides in the ODS-T250 steel hindered shear, which required a greater driving force for martensite transformation and thus contributed to the decrease in the Ms temperature. The decrease in Ms temperature caused by second-phase particles has been well-documented in previous studies. For instance, the formation of coherent γ'-$(Ni,Fe)_3Si$ precipitates with an $L1_2$ structure in Fe–Ni–Si alloys reduced the Ms temperature by 56 °C. This reduction was attributed to the additional driving force required for the stress-induced transformation of the γ'-$(Ni,Fe)_3Si$ precipitates [61]. Similarly, the precipitation of γ'-Ni_3Ti in Fe–31Ni–3Ti alloys resulted in a significant reduction of 115 K in the Ms temperature [62]. More dramatically, Fe–28Ni–12Al alloys exhibited a large decrease of 208 °C in the Ms temperature due to the precipitation of Ni_3Al [63]. These studies consistently demonstrate that the precipitation of second-phase particles within the austenite matrix hinders the martensitic formation, as evidenced by the decrease in Ms temperature.

Table 4
Values of k_i for the main alloying elements in the current steels.

Element	Ni	Mo	Ti
k_i	−15.5	−10.7	3.0

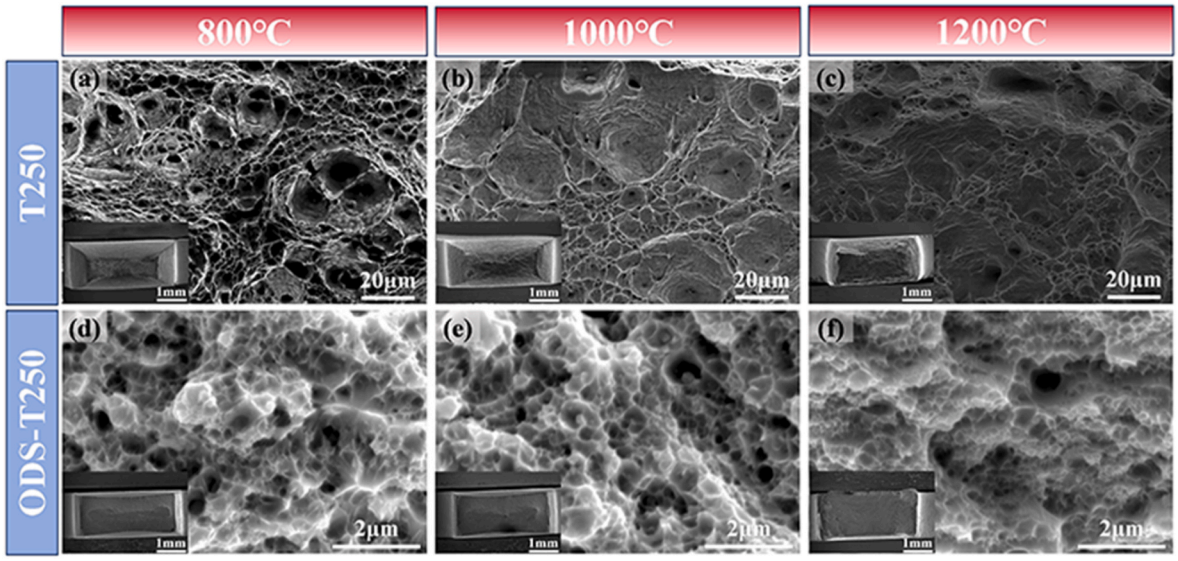

Fig. 13. Tensile fracture morphology of (a–c) T250 and (d–f) ODS-T250 steels: (a) and (d) quenched from 800 °C, (b) and (e) quenched from 1000 °C, (c) and (f) quenched from 1200 °C.

4.3. Strengthening mechanism in ODS-T250 steel

As shown in Fig. 12, both tensile strength and yield strength of the ODS-T250 steel were higher than those of T250 steel. The strength decreased with an increasing solid solution temperature, with the highest strength obtained when quenched from 800 °C. After quenching from 800 °C, the yield strength of the T250 steel was 793 MPa, whereas that of the ODS-T250 steel reached 959 MPa, increasing by nearly 20 %. Therefore, the strengthening contributions were analyzed and quantified. Typically, the strength of martensitic steels primarily stems from the contribution of friction stress in pure iron (σ_0), solid solution strengthening (σ_{ss}) which arises from the interaction between dislocations and solutes, grain boundary strengthening (σ_{gb}) due to the inhibiting effect of grain boundaries on dislocation movement, dislocation strengthening (σ_{dis}) resulting from interactions in the dislocation strain fields, and precipitation strengthening (σ_p) caused by the inhibiting effect of precipitates on dislocation movement. Therefore, the yield strength (σ_y) of the T250 and ODS-T250 steels can be calculated using the following equation [64]:

$$\sigma_y = \sigma_0 + \sigma_{ss} + \sigma_{gb} + \sqrt{\sigma_{dis}^2 + \sigma_p^2} \tag{3}$$

The friction stress in pure iron (σ_0) is taken as 54 MPa [65]. Solid solution strengthening in steels can be calculated using the following equation [66,67]:

$$\sigma_{ss} = \sum K_i c_i^z \tag{4}$$

where K_i is a hardening constant and c_i is the atomic percent of substitutional elements. The exponent z is equal to 0.75 [66,67]. The value of K_i is 19.2, 17.9 and 15.9 MPa/at%$^{-3/4}$ corresponding to the elements Ni, Ti, and Mo, respectively [68].

The yield strength contributed by grain boundaries can be explained by the Hall-Petch relationship [69]:

$$\sigma_{gb} = k_y d^{-1/2} \tag{5}$$

where k_y is Hall-Petch coefficient and d represents the average of effective grain size.

In this work, the block width is considered as the effective grain size of the T250 steel [70], while the PAGS size is considered as the effective grain size of ODS-T250. The constant k_y is taken as 120 MPa/μm$^{1/2}$ [71].

As for dislocation strengthening, it can be expressed as follows:

$$\sigma_{dis} = M\alpha Gb\sqrt{\rho} \tag{6}$$

where M is the Taylor factor (3.0) [72], G is the shear modulus of iron (80 GPa) [72], b is the Burgers vector (0.25 nm) [72], α is a constant (0.13) [73], and ρ is the dislocation density.

Precipitation strengthening of dispersed oxides in ODS alloys is based on the Orowan looping mechanism, which can be expressed by the following equation [74]:

$$\sigma_p = \frac{0.81MGb}{2\pi\sqrt{1-\nu}} \frac{\ln\left(\frac{2\sqrt{2/3}\cdot r}{2b}\right)}{\left(\sqrt{2\pi/3f}\cdot r\right)} \tag{7}$$

where r and f represent the mean radius and volume fraction of oxide nanoparticles, respectively. Poisson's ratio (ν) is taken as 0.3 [75].

Fig. 14 compares the measured value and calculated value of yield strength in two steels. The experimental results aligned well with the calculated strengthening contributions for both steels. However, the difference between the experimental value and the calculated value was more pronounced in the ODS-T250 steel than in the T250 steel. It was evident that solid solution strengthening and dislocation strengthening contributed the most to the yield strength of both the T250 and ODS-T250 steels. Additionally, due to the ultrafine grain and dispersed oxides in the ODS-T250 steel, grain boundary strengthening and precipitation strengthening increased by 166 and 87 MPa, respectively, resulting in a significant enhancement in yield strength.

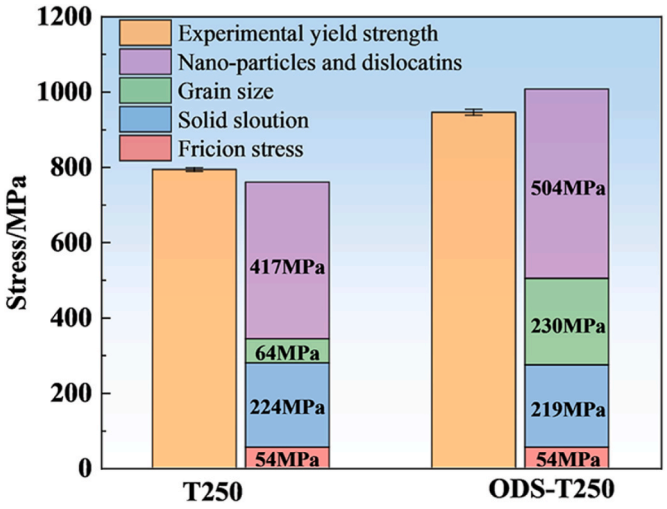

Fig. 14. Different strengthening contributions to the yield strength in the T250 and ODS-T250 steels quenched from 800 °C.

5. Conclusion

In this study, ultrafine-grained ODS-T250 maraging steel was prepared by mechanical ball milling and hot isostatic pressing. The main results can be summarized as follows:

(1) ODS-T250 steel exhibits excellent structural thermal stability, maintaining an effective grain size of 0.348 μm even after quenching from 1200 °C, compared to 5.473 μm in T250 steel. Moreover, the martensite morphology is equiaxed in ODS-T250 steel, whereas it is lath-type in T250 steel.
(2) As the PAGS decreased, variant selectivity increased, while the number of variants within a single prior austenite grain decreased. When the PAGS is smaller than 0.43 μm, only a single variant forms per prior austenite grain.
(3) The refinement of PAGS and oxides jointly contributed to the decrease in Ms temperature.
(4) Irrespective of the solid-solution temperature, both the strength and ductility were improved in the ODS-T250 steel compared with the T250 steel. Grain boundary strengthening and oxide dispersion strengthening were the primary contributors to the increased strength of the ODS-T250 steel.

Data availability

Data will be made available on request.

Declaration of competing interest

The authors declare that they have no known competing financial interests or personal relationships that could have appeared to influence the work reported in this paper.

References

[1] Zeisl S, Landefeld A, Van Steenberge N, Chang Y, Schnitzer R. The role of alloying elements in NiAl and Ni3Ti strengthened Co-free maraging steels. Mater Sci Eng, A 2022;861:144313. https://doi.org/10.1016/j.msea.2022.144313.
[2] Li K, Yu B, Misra RDK, Han G, Liu S, Shang CJ. Strengthening of cobalt-free 19Ni3Mo1.5Ti maraging steel through high-density and low lattice misfit

nanoscale precipitates. Mater Sci Eng, A 2018;715:174–85. https://doi.org/10.1016/j.msea.2017.12.109.
[3] Jiang S, Wang H, Wu Y, Liu X, Chen H, Yao M, et al. Ultrastrong steel via minimal lattice misfit and high-density nanoprecipitation. Nature 2017;544:460–4. https://doi.org/10.1038/nature22032.
[4] Simm TH, Sun L, Galvin DR, Hill P, Rawson M, Birosca S, et al. The effect of a two-stage heat-treatment on the microstructural and mechanical properties of a maraging steel. Materials 2017;10:1346. https://doi.org/10.3390/ma10121346.
[5] Zhang H, Sun M, Liu Y, Ma D, Xu B, Huang M, et al. Ultrafine-grained dual-phase maraging steel with high strength and excellent cryogenic toughness. Acta Mater 2021;211:116878. https://doi.org/10.1016/j.actamat.2021.116878.
[6] Marcisz J, Adamczyk M, Garbarz B. Optimisation of mechanical properties of 18% Ni350 Grade maraging steel using novel heat treatment. Arch Metall Mater 2017;62:73–84. https://doi.org/10.1515/amm-2017-0010.
[7] Wan J, Ruan H, Ding Z, Kong LB. A novel maraging stainless steel ultra-high-strengthened by multi-nanoprecipitations. Scr Mater 2023;226:115224. https://doi.org/10.1016/j.scriptamat.2022.115224.
[8] Li W, Ding Q, Wei X, Zhang Z, Bei H. Achieving the strength and ductility synergy in a steel through nanoprecipitation and its induced grain refinement. Mater Today 2025;83:213–22. https://doi.org/10.1016/j.mattod.2025.01.004.
[9] Zeisl S, Lassnig A, Hohenwarter A, Mendez-Martin F. Precipitation behavior of a Co-free Fe-Ni-Cr-Mo-Ti-Al maraging steel after severe plastic deformation. Mater Sci Eng, A 2022;833:142416. https://doi.org/10.1016/j.msea.2021.142416.
[10] Zeng T, Luo Z, Chen H, Wang W, Yang K. Flow behavior and dynamic recrystallization mechanism of CSS-42L bearing steel during hot compression deformation. Acta Metall Sin 2024. https://doi.org/10.1007/s40195-024-01797-8.
[11] Zhou X, Jia C, Mi P, Zhang H, Yan W, Wang W, et al. Cyclic quenching treatment doubles the Charpy V-notch impact energy of a 2.3 GPa maraging steel. J Mater Sci Technol 2025;209:311–28. https://doi.org/10.1016/j.jmst.2024.05.026.
[12] Wang Z, Gu X, Pan H. Cyclic quenching treatment to improve strength–ductility combinations in 18CrNiMo7-6 steel. J Mater Eng Perform 2024;33:10446–54. https://doi.org/10.1007/s11665-023-08692-w.
[13] Javadzadeh Kalahroudi F, Koohdar H, Langdon TG, Nili-Ahmadabadi M. Phase evolution and mechanical properties of an intercritically-annealed Fe–10Ni–7Mn (wt. %) martensitic steel severely deformed by high-pressure torsion. Mater Sci Eng, A 2021;804:140519. https://doi.org/10.1016/j.msea.2020.140519.
[14] Yang MX, Yang G, Liu ZD, Wang C, Huang CX. Significant enhancement of strength in a lamellar-type nanostructured maraging steel subjected to equal-channel angular pressing for 12 passes. Mater Sci Eng, A 2012;550:429–33. https://doi.org/10.1016/j.msea.2012.04.014.
[15] Tirekar S, Jafarian HR, Eivani AR. Towards engineering of mechanical properties through stabilization of austenite in ultrafine grained martensite–austenite dual phase steel processed by accumulative roll bonding. Mater Sci Eng, A 2017;684:120–6. https://doi.org/10.1016/j.msea.2016.12.039.
[16] Langdon TG, Furukawa M, Nemoto M, Horita Z. Using equal-channel angular pressing for refining grain size. JOM 2000;52:30–3. https://doi.org/10.1007/s11837-000-0128-7.
[17] Zhang LX, Liu L, Guo S, Pan QS, Lu L. Microstructure and evolution of gradient dislocation cells in multi-principal element alloy subjected to cyclic torsion. Acta Mater 2024;275:120059. https://doi.org/10.1016/j.actamat.2024.120059.
[18] Yuan Q, Li Z, Zhang Q, Xu G. Towards excellent strength-ductility synergy via high temperature short time annealing in low-carbon ultrafine grain steel. Mater Sci Eng, A 2023;886:145674. https://doi.org/10.1016/j.msea.2023.145674.
[19] Zhao Z, Cao Y, Zhang Y, Fu A, Zhang R, Zhong Y, et al. Creep behavior of a novel ODS ferrite steel reinforced with ultra-fine Y2(Zr0.6, Ti0.4)2O7 particles. Mater Char 2024;215:114231. https://doi.org/10.1016/j.matchar.2024.114231.
[20] Deng L, Luo J, Tu J, Hu R, Guo N, Zeng W, et al. Achieving excellent mechanical properties of ODS steel by Y2O3 addition. Mater Sci Eng, A 2023;872:145008. https://doi.org/10.1016/j.msea.2023.145008.
[21] Oñoro M, de Castro V, Leguey T, Pöpperlová J, Huizenga RM, Auger MA. Microstructural stability of secondary phases in an ODS ferritic steel after thermal aging at 873 K. Mater Char 2024;207:113517. https://doi.org/10.1016/j.matchar.2023.113517.
[22] Zeng T. On the martensitic structure and hardness in as-quenched Fe-Ni alloys. J Alloys Compd 2022;894:143042. https://doi.org/10.1016/j.jallcom.2017.08.285.
[23] Morito S, Tanaka H, Konishi R, Furuhara T, Maki T. The morphology and crystallography of lath martensite in Fe-C alloys. Acta Mater 2003;51:1789–99. https://doi.org/10.1016/S1359-6454(02)00577-3.
[24] Morito S, Saito H, Ogawa T, Furuhara T, Maki T. Effect of austenite grain size on the morphology and crystallography of lath martensite in low carbon steels. ISIJ Int 2005;45:91–4. https://doi.org/10.2355/isijinternational.45.91.
[25] Niessen F, Nyyssönen T, Gazder AA, Hielscher R. Parent grain reconstruction from partially or fully transformed microstructures in *MTEX*. J Appl Crystallogr 2022;55:180–94. https://doi.org/10.1107/S1600576721011560.
[26] Ribárik G, Ungár T, Gubicza J. MWP-fit: a program for multiple whole-profile fitting of diffraction peak profiles by ab initio theoretical functions. J Appl Crystallogr 2001;34:669–76. https://doi.org/10.1107/S0021889801011451.
[27] Zeng T, Zhang S, Shi X, Wang W, Yan W, Yang K. Effect of NbC and VC carbides on microstructure and strength of high-strength low-alloyed steels for oil country tubular goods. Mater Sci Eng, A 2021;824:141845. https://doi.org/10.1016/j.msea.2021.141845.
[28] Liu G, Sun J, Nan C-W, Chen K-H. Experiment and multiscale modeling of the coupled influence of constituents and precipitates on the ductile fracture of heat-treatable aluminum alloys. Acta Mater 2005;53:3459–68. https://doi.org/10.1016/j.actamat.2005.04.002.
[29] Zhao YY, Chen HW, Lu ZP, Nieh TG. Thermal stability and coarsening of coherent particles in a precipitation-hardened (NiCoFeCr)94Ti2Al4 high-entropy alloy. Acta Mater 2018;147:184–94. https://doi.org/10.1016/j.actamat.2018.01.049.
[30] Guo F, Zhang C, Zhai Y, Cheng Q, Wang M, Wang Q, et al. Nanosized austenite and coherent nanoprecipitates making maraging steel strong and ductile. Mater Sci Eng, A 2024;902:146605. https://doi.org/10.1016/j.msea.2024.146605.
[31] Maki T. 2 - morphology and substructure of martensite in steels. In: Pereloma E, Edmonds DV, editors. Phase transformations in steels, vol. 2. Woodhead Publishing; 2012. p. 34–58. https://doi.org/10.1533/9780857096111.1.34.
[32] Morito S, Huang X, Furuhara T, Maki T, Hansen N. The morphology and crystallography of lath martensite in alloy steels. Acta Mater 2006;54:5323–31. https://doi.org/10.1016/j.actamat.2006.07.009.
[33] Truong TD, Asala G, Ola OT, Ojo OA, Odeshi AG. Effects of additive manufacturing process parameters and heat treatment on texture evolution and variant selection during austenite-martensite transformation in 18%Ni-M350 maraging steel. Mater Char 2023;204:113190. https://doi.org/10.1016/j.matchar.2023.113190.
[34] Long S, Liang Y, Jiang Y, Liang Y, Yang M, Yi Y. Effect of quenching temperature on martensite multi-level microstructures and properties of strength and toughness in 20CrNi2Mo steel. Mater Sci Eng, A 2016;676:38–47. https://doi.org/10.1016/j.msea.2016.08.065.
[35] Zhang H, Ji X, Ma D, Tong M, Wang T, Xu B, et al. Effect of aging temperature on the austenite reversion and mechanical properties of a Fe–10Cr–10Ni cryogenic maraging steel. J Mater Res Technol 2021;11:98–111. https://doi.org/10.1016/j.jmrt.2020.12.096.
[36] Yang T, Dou P, Zhang P, Yang Y. STEM and HRTEM study on matrix microstructure and oxide particles in 11Cr ferritic/martensitic ODS steel. J Nucl Mater 2023;576:154259. https://doi.org/10.1016/j.jnucmat.2023.154259.
[37] Wu Y, Ciston J, Kräemer S, Bailey N, Odette GR, Hosemann P. The crystal structure, orientation relationships and interfaces of the nanoscale oxides in nanostructured ferritic alloys. Acta Mater 2016;111:108–15. https://doi.org/10.1016/j.actamat.2016.03.031.
[38] Kurdjumov G. Over the mechanisms of steel hardening. Z Phys 1930;64:325.
[39] Nishiyama Z. X-ray investigation of the mechanism of the transformation from face centered cubic lattice to body centered cubic. Sci Rep Tohoku Univ 1934;23:637.
[40] Wassermann G. Einfluß der α-γ-Umwandlung eines irreversiblen Nickelstahls auf Kristallorientierung und Zugfestigkeit. Arch für das Eisenhuttenwes 1933;6:347–51. https://doi.org/10.1002/srin.193300427.
[41] Krauss G, editor. Steels: processing, structure, and performance. second ed. Materials Park: ASM International; 2015.
[42] Morito S, Yoshida S, Hayamizu R, Hayashi T, Ohba T, Terasaki H, et al. Three-dimensional approach to observing growth of blocks and packets in Fe-18Ni maraging steel. Mater Sci Forum 2014;783–786:916–9. https://doi.org/10.4028/www.scientific.net/MSF.783-786.916.
[43] Morito S, Igarashi R, Kamiya K, Ohba T, Maki T. Effect of cooling rate on morphology and crystallography of lath martensite in Fe-Ni alloys. Materials Science Forum - MATER SCI FORUM 2010;638–642:1459–63. https://doi.org/10.4028/www.scientific.net/MSF.638-642.1459.
[44] Ji H, Wang J, Wang Z, Li Y. Effect of martensitic variant selection on the crystallographic features of bainite/martensite multiphase structure of 42CrMo steel. J Mater Res Technol 2024;30:9561–71. https://doi.org/10.1016/j.jmrt.2024.06.049.
[45] Wang K, Hu F, Zhou S, Zhou W, Hu C, Yershov S, et al. Microstructural evolution and ultra-high impact toughness of austempered lamellar bainitic steel far below Ms temperature. J Mater Res Technol 2023;24:5449–62. https://doi.org/10.1016/j.jmrt.2023.04.172.
[46] Takayama N, Miyamoto G, Furuhara T. Effects of transformation temperature on variant pairing of bainitic ferrite in low carbon steel. Acta Mater 2012;60:2387–96. https://doi.org/10.1016/j.actamat.2011.12.018.
[47] Nishizawa T, Ohnuma I, Ishida K. Examination of the zener relationship between grain size and particle dispersion. Mater Trans JIM 1997;38:950–6. https://doi.org/10.2320/matertrans1989.38.950.
[48] Huang C-Y, Lu S-L, Yen H-W. Digital reconstruction of engineered austenite: revisiting effects of grain size and ausforming on variant selection of martensite. Metals 2022;12:1511. https://doi.org/10.3390/met12091511.
[49] Zhao J, Hou Z, Wang B, Yang H, Wang Y, Chang Z, et al. Effect of austenitizing temperature on variant selection of martensite transformation in a 2 GPa grade steel. J Mater Res Technol 2024;33:2794–802. https://doi.org/10.1016/j.jmrt.2024.10.008.
[50] Celada-Casero C, Sietsma J, Santofimia MJ. The role of the austenite grain size in the martensitic transformation in low carbon steels. Mater Des 2019;167:107625. https://doi.org/10.1016/j.matdes.2019.107625.
[51] Yin TW, Shen YF, Jia N, Li YJ, Xue WY. Controllable selection of martensitic variant enables concurrent enhancement of strength and ductility in a low-carbon steel. Int J Plast 2023;168:103704. https://doi.org/10.1016/j.ijplas.2023.103704.
[52] Hanamura T, Torizuka S, Tamura S, Enokida S, Takechi H. Effect of austenite grain size on transformation behavior, microstructure and mechanical properties of 0.1C–5Mn martensitic steel. ISIJ Int 2013;53:2218–25. https://doi.org/10.2355/isijinternational.53.2218.
[53] Brofman PJ, Ansell GS. On the effect of fine grain size on the Ms temperature in Fe-27Ni-0.025C alloys. Metall Trans A 1983;14:1929–31. https://doi.org/10.1007/BF02645565.
[54] Kaar S, Steineder K, Schneider R, Krizan D, Sommitsch C. New Ms-formula for exact microstructural prediction of modern 3rd generation AHSS chemistries. Scr Mater 2021;200:113923. https://doi.org/10.1016/j.scriptamat.2021.113923.
[55] Umemoto M, Owen WS. Effects of austenitizing temperature and austenite grain size on the formation of athermal martensite in an iron-nickel and an iron-nickel-

carbon alloy. Metall Trans A 1974;5:2041–6. https://doi.org/10.1007/BF02644497.
[56] Lee SJ, Lee Y-K. Effect of austenite grain size on martensitic transformation of a low alloy steel. MSF 2005;475–479:3169–72. https://doi.org/10.4028/www.scientific.net/MSF.475-479.3169.
[57] Jimenez-Melero E, van Dijk NH, Zhao L, Sietsma J, Offerman SE, Wright JP, et al. Martensitic transformation of individual grains in low-alloyed TRIP steels. Scr Mater 2007;56:421–4. https://doi.org/10.1016/j.scriptamat.2006.10.041.
[58] García-Junceda A, Capdevila C, Caballero FG, de Andrés CG. Dependence of martensite start temperature on fine austenite grain size. Scr Mater 2008;58:134–7. https://doi.org/10.1016/j.scriptamat.2007.09.017.
[59] Yang H, Bhadeshia H. Austenite grain size and the martensite-start temperature. Scr Mater 2009;60:493–5. https://doi.org/10.1016/j.scriptamat.2008.11.043.
[60] Lee S-J, Park K-S. Prediction of martensite start temperature in alloy steels with different grain sizes. Metall Mater Trans A 2013;44:3423–7. https://doi.org/10.1007/s11661-013-1798-4.
[61] Himuro Y, Kainuma R, Ishida K. Martensitic transformation and shape memory effect in ausaged Fe–Ni–Si alloys. ISIJ Int 2002;42:184–90. https://doi.org/10.2355/isijinternational.42.184.
[62] Maki T, Kobayashi K, Tamura I. Effect of ausaging on the moorphology of martensite in Fe-Ni-Ti-Co alloys. J Phys Colloq 1982;43:C4–546. https://doi.org/10.1051/jphyscol:1982484.
[63] Hornbogen E, Meyer W. Martensitische Umwandlung von Mischkristallen mit kohärenten Teilchen. Acta Metall 1967;15:584–6. https://doi.org/10.1016/0001-6160(67)90099-5.
[64] Zhou X, Liu Y, Yu L, Ma Z, Guo Q, Huang Y, et al. Microstructure characteristic and mechanical property of transformable 9Cr-ODS steel fabricated by spark plasma sintering. Mater Des 2017;132:158–69. https://doi.org/10.1016/j.matdes.2017.06.063.
[65] Zeng TY, Li W, Wang NM, Wang W, Yang K. Microstructural evolution during tempering and intrinsic strengthening mechanisms in a low carbon martensitic stainless bearing steel. Mater Sci Eng, A 2022;836:142736. https://doi.org/10.1016/j.msea.2022.142736.
[66] Dadé M, Malaplate J, Garnier J, De Geuser F, Barcelo F, Wident P, et al. Influence of microstructural parameters on the mechanical properties of oxide dispersion strengthened Fe-14Cr steels. Acta Mater 2017;127:165–77. https://doi.org/10.1016/j.actamat.2017.01.026.
[67] Shen J, Li Y, Li F, Yang H, Zhao Z, Kano S, et al. Microstructural characterization and strengthening mechanisms of a 12Cr-ODS steel. Mater Sci Eng, A 2016;673:624–32. https://doi.org/10.1016/j.msea.2016.07.030.
[68] Lu Q, Xu W, Zwaag S van der. Designing new corrosion resistant ferritic heat resistant steel based on optimal solid solution strengthening and minimisation of undesirable microstructural components. Comput Mater Sci 2014;84:198–205. https://doi.org/10.1016/j.commatsci.2013.12.009.
[69] Ren J, Li C, Han Y, Li E, Gao C, Qiu C. Effect of initial martensite and tempered carbide on mechanical properties of 3Cr2MnNiMo mold steel. Mater Sci Eng, A 2021;812:141080. https://doi.org/10.1016/j.msea.2021.141080.
[70] Morito S, Yoshida H, Maki T, Huang X. Effect of block size on the strength of lath martensite in low carbon steels. Mater Sci Eng, A 2006;438–440:237–40. https://doi.org/10.1016/j.msea.2005.12.048.
[71] Kim B, Boucard E, Sourmail T, San Martín D, Gey N, Rivera-Díaz-del-Castillo PEJ. The influence of silicon in tempered martensite: understanding the microstructure–properties relationship in 0.5–0.6 wt.% C steels. Acta Mater 2014;68:169–78. https://doi.org/10.1016/j.actamat.2014.01.039.
[72] Jiao ZB, Luan JH, Miller MK, Yu CY, Liu Y, Liu CT. Precipitate transformation from NiAl-type to Ni2AlMn-type and its influence on the mechanical properties of high-strength steels. Acta Mater 2016;110:31–43. https://doi.org/10.1016/j.actamat.2016.03.024.
[73] Li Z, Chai F, Yang L, Luo X, Yang C. Mechanical properties and nanoparticles precipitation behavior of multi-component ultra high strength steel. Mater Des 2020;191:108637. https://doi.org/10.1016/j.matdes.2020.108637.
[74] Wu S, Li J, Li C, Li Y, Xiong L, Liu S. Preliminary study on the fabrication of 14Cr-ODS FeCrAl alloy by powder forging. J Mater Sci Technol 2021;83:49–57. https://doi.org/10.1016/j.jmst.2020.12.032.
[75] Zhou T, Lu J, Hedström P. Mechanical behavior of fresh and tempered martensite in a CrMoV-alloyed steel explained by microstructural evolution and strength modeling. Metall Mater Trans A 2020;51:5077–87. https://doi.org/10.1007/s11661-020-05922-x.